nature materials

LETTERS

PUBLISHED ONLINE: 12 OCTOBER 2014 | DOI: 10.1038/NMAT4107

Giant spin splitting of the two-dimensional electron gas at the surface of $SrTiO_3$

A. F. Santander-Syro[1]*, F. Fortuna[1], C. Bareille[1], T. C. Rödel[1,2], G. Landolt[3,4], N. C. Plumb[4], J. H. Dil[3,4,5]* and M. Radović[4,5,6]*

Two-dimensional electron gases (2DEGs) forming at the interfaces of transition metal oxides[1–3] exhibit a range of properties, including tunable insulator–superconductor–metal transitions[4–6], large magnetoresistance[7], coexisting ferromagnetism and superconductivity[8,9], and a spin splitting of a few meV (refs 10,11). Strontium titanate ($SrTiO_3$), the cornerstone of such oxide-based electronics, is a transparent, non-magnetic, wide-bandgap insulator in the bulk, and has recently been found to host a surface 2DEG (refs 12–15). The most strongly confined carriers within this 2DEG comprise two subbands, separated by an energy gap of 90 meV and forming concentric circular Fermi surfaces[12,13,15]. Using spin- and angle-resolved photoemission spectroscopy (SARPES), we show that the electron spins in these subbands have opposite chiralities. Although the Rashba effect might be expected to give rise to such spin textures, the giant splitting of almost 100 meV at the Fermi level is far larger than anticipated[16,17]. Moreover, in contrast to a simple Rashba system, the spin-polarized subbands are non-degenerate at the Brillouin zone centre. This degeneracy can be lifted by time-reversal symmetry breaking, implying the possible existence of magnetic order. These results show that confined electronic states at oxide surfaces can be endowed with novel, non-trivial properties that are both theoretically challenging to anticipate and promising for technological applications.

The 2DEG at the surface of $SrTiO_3$, formed by confined electrons of the t_{2g} conduction band with Ti-3*d* character, is universal in the sense that its constituent subbands, their fillings, and their Fermi surfaces are independent of the bulk sample doping and of whether the surfaces are prepared by cleaving[12,13] or by etching and *in situ* annealing[15]. This 2DEG consists of two light electron subbands dispersing down to about −180 meV and −90 meV, respectively, below the Fermi level (E_F), producing concentric Fermi surfaces around the Brillouin zone centre, and heavy shallow subbands dispersing down to about −40 meV, forming ellipsoidal Fermi surfaces[12,13,15].

In fact, the 2DEG in $SrTiO_3$ has been associated with a band bending of ∼300 meV at the surface of the material[12,13,15]. In such a quantum well profile, the most bound light subbands are tightly confined near the surface, whereas the less bound heavy subbands are more delocalized towards the bulk[12,15]. The present work focuses on resolving the spin structure of the strongly two-dimensional light subbands, which are the most technologically relevant in terms of their carrier concentration and mobility.

The surface band bending of ∼300 meV amounts to an electric field $\mathcal{F} \sim 100\ \mathrm{MV\,m^{-1}}$ confining the conduction electrons near the surface. In a simple approximation, this field will induce a so-called 'Rashba splitting' of the spin states in each subband, with the largest splitting occurring for the most bound subbands. In an ideal surface, the corresponding momentum separation (k_R) will be of the order of $k_R \approx 2e\mathcal{F}/\Delta$, where Δ is the gap between the valence and conduction bands[14,18]. For $\mathcal{F} \sim 100\ \mathrm{MV\,m^{-1}}$ and $\Delta \sim 3.5$ eV, typical of the 2DEG at the surface of $SrTiO_3$ (refs 12,15), the momentum spin splitting at E_F is thus expected to be of the order of $k_R \sim 6 \times 10^{-3}\ \mathrm{Å^{-1}}$, at the limit of the best resolutions today available in ARPES. For the light subbands in $SrTiO_3$, such momentum splitting amounts to an energy splitting of a few meV near E_F, as indeed inferred from magnetotransport measurements in the 2DEG at $LaAlO_3/SrTiO_3$ interfaces subject to a strong voltage bias[10,11], and also predicted by *ab initio* calculations of the 2DEG at such interfaces[16,17]. However, the possible spin splitting of the 2DEG at the surface of $SrTiO_3$ has not been measured so far.

As we will see next, in marked contrast to the above expectations, our data reveal an astounding discovery: first, each of the light subbands of the 2DEG at the surface of $SrTiO_3$ is spin-polarized, with spins winding in helical texture around the Fermi surface, such that the momentum spin splitting is one order of magnitude larger than the one estimated above; second, the electronic structure is gapped at $\mathbf{k}=0$, which is not expected in a simple Rashba picture.

For our experiments, we prepared the 2DEG *in situ* on (001)-oriented TiO_2-terminated surfaces of $SrTiO_3$ (ref. 15; Methods). This produces pristine monocrystalline surfaces showing a 2DEG with light and heavy subbands (Supplementary Note 1), identical to those observed in cleaved $SrTiO_3$ surfaces[12,13], but with much sharper photoemission lines and a larger signal-to-background ratio, which are crucial for SARPES measurements. For reasons explained earlier, we focus henceforth on the two lowest light subbands. To this end, we take advantage of the fact that the photoemission signal from the heavy subbands can be 'silenced' by dipole-transition selection rules, through a combination of experimental geometry and light energy and polarization, leaving only the light subbands, as fully documented in ref. 12 (see also Supplementary Note 1).

The geometry of the experimental set-up is schematically shown in Fig. 1a. Figure 1b shows the circular Fermi surfaces of the 2DEG, measured in spin-integrated mode with the Channeltron detectors of the SARPES set-up. These Fermi surfaces are generated by two

[1]CSNSM, Université Paris-Sud and CNRS/IN2P3, Bâtiments 104 et 108, 91405 Orsay cedex, France. [2]Synchrotron SOLEIL, L'Orme des Merisiers, Saint-Aubin-BP48, 91192 Gif-sur-Yvette, France. [3]Physik-Institut, Universität Zürich, Winterthurerstrasse 190, 8057 Zürich, Switzerland. [4]Swiss Light Source, Paul Scherrer Institut, CH-5232 Villigen PSI, Switzerland. [5]Institute of Condensed Matter Physics, Ecole Polytechnique Fédérale de Lausanne, CH-1015 Lausanne, Switzerland. [6]SwissFEL, Paul Scherrer Institut, CH-5232 Villigen PSI, Switzerland. *e-mail: andres.santander@csnsm.in2p3.fr; hugo.dil@epfl.ch; milan.radovic@psi.ch

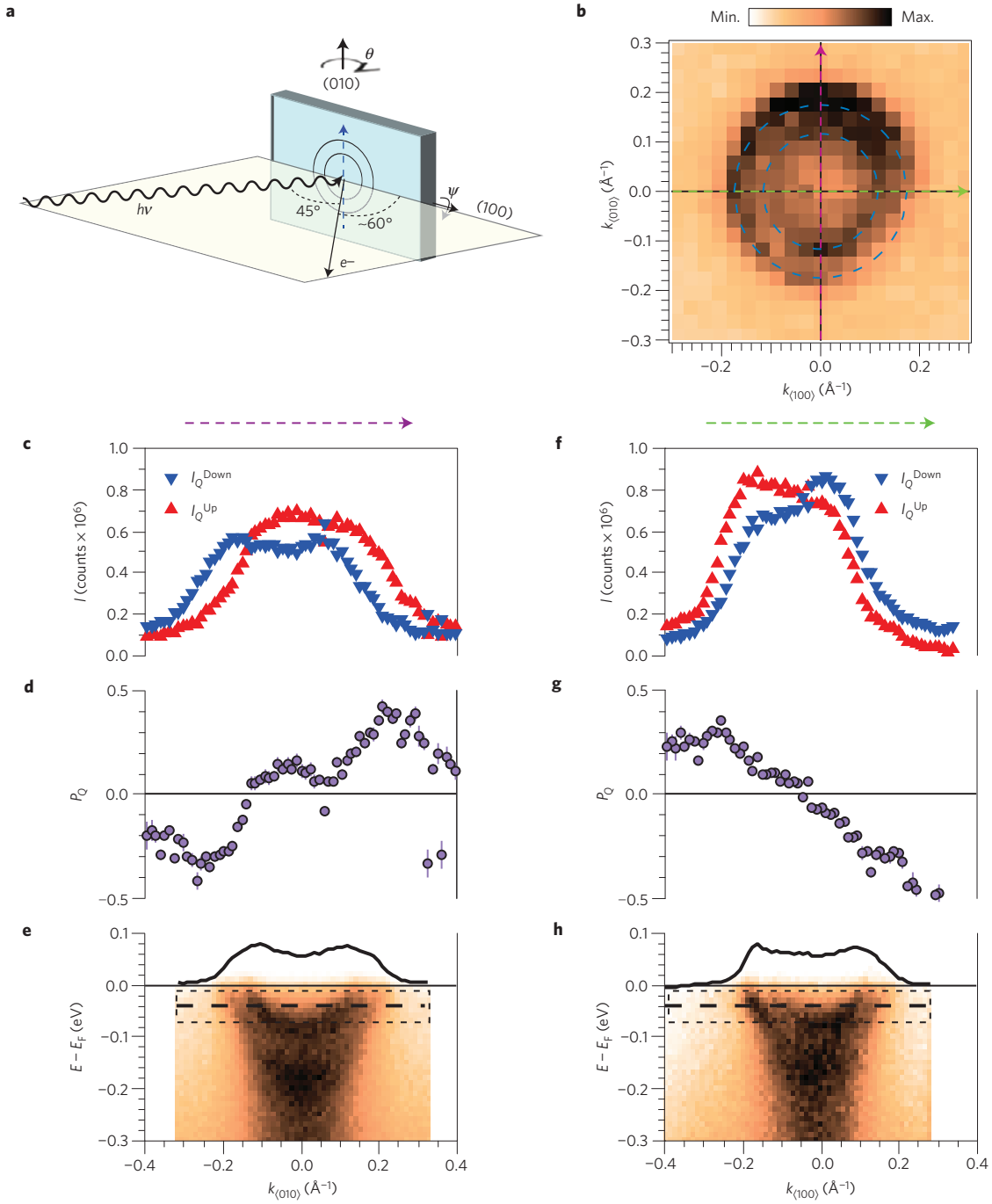

Figure 1 | Spin-polarized subbands of the 2DEG at the surface of $SrTiO_3$. a, Schematic experimental geometry. The incident light beam (energy $h\nu$) and the outgoing electrons entering the detector define the scattering plane, horizontal in this case. Light polarization (horizontal or vertical) is referred to this plane. Reciprocal space along (100) and (010) is explored by varying, respectively, the angles θ and ψ. **b**, ARPES Fermi surface map of the 2DEG in $SrTiO_3$. The dashed blue circles are guides to the eye for the two Fermi surfaces generated by the light parabolic subbands. **c**, Spin-resolved populations of spin-up and spin-down electrons (with respect to **Q**) around the Fermi level, as a function of electron momentum along (010). SARPES data were measured within the Gaussian resolution-broadened energy range indicated by the dashed rectangle in **e**. **d**, Resulting angle-resolved spin polarization around E_F along the local spin quantization axis *Q*. **e**, Energy–momentum intensity map along (010), violet dashed arrow in **b**, showing the two light subbands. The dashed rectangle and bold line in this and other figures indicate the Gaussian energy broadening and energy setting for the SARPES measurements. The black curve on top of the colour plot is the ARPES momentum distribution curve (MDC) integrated over the dashed rectangle. **f**–**h** same as **c**–**e** along the orthogonal momentum direction (100), green dashed arrow in **b**. Note from **a** that the angular movements θ and ψ are not equivalent with respect to the scattering plane, causing differences in the shape of the spin polarizations along (100) and (010). All data in this figure were measured at $T = 20$ K using linear-vertical photons at $h\nu = 47$ eV, around angles $\theta = 60°$ and $\psi = 0$ as depicted in **a**, corresponding to the Γ_{102} Brillouin zone.

light parabolic subbands, whose dispersions along the (010) and (100) directions in reciprocal space are shown by the colour plots in Fig. 1e,h.

We now discuss our spin-resolved measurements near the Fermi level (E_F). Figure 1c shows the populations of electrons with momentum along (010) having their spin parallel (up) or

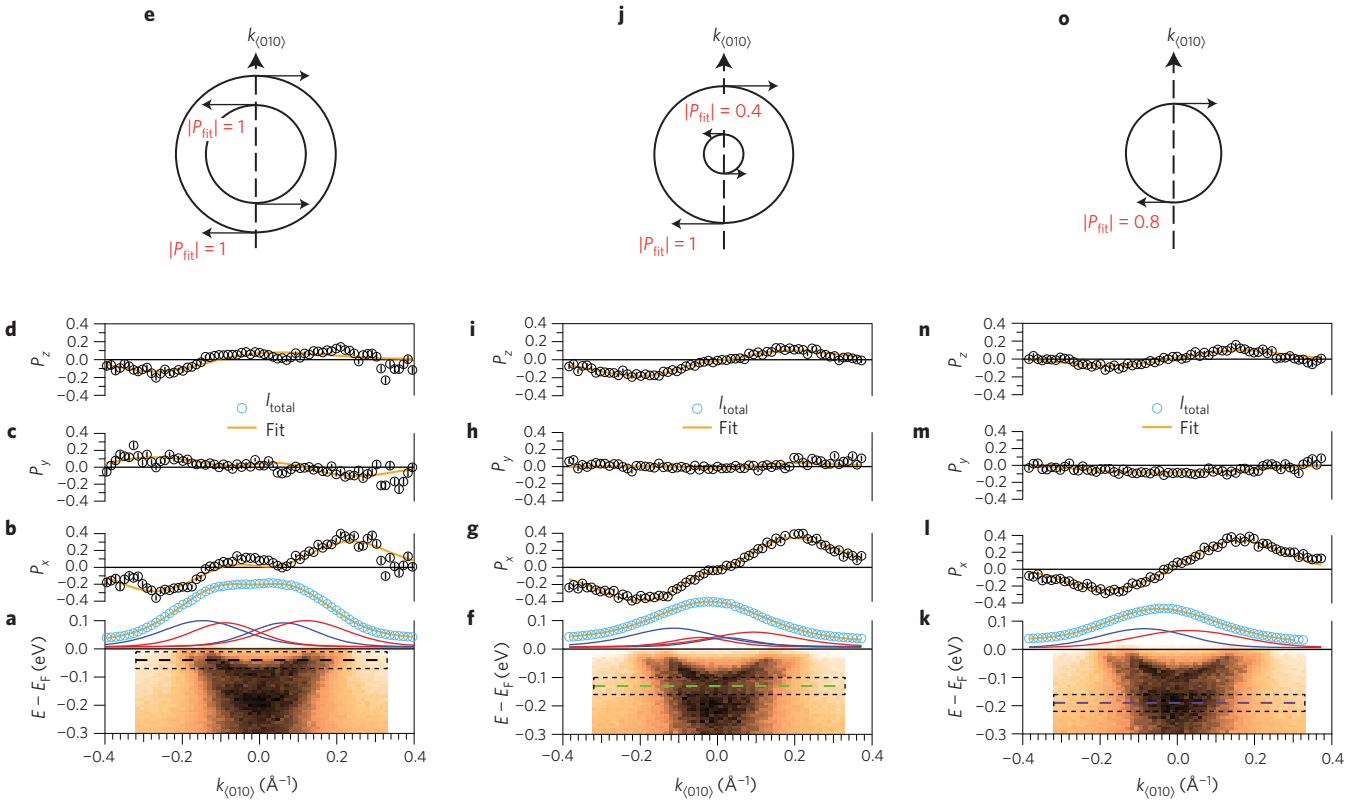

Figure 2 | Spin components at different subband binding energies. a, Energy–momentum intensity map along (010) (colour plot), and MDC of the total spin-integrated signal (blue circles) recorded by the Mott detectors over the resolution-broadened energy range indicated by the dashed rectangle. **b–d**, Corresponding angle-resolved spin polarizations (black circles) along the local *x* (tangential to the Fermi surface), *y* (radial) and *z* (out-of-plane) axes, respectively. The red and blue curves in **a** are Voigt fits for the spin-up and spin-down population fitting simultaneously (orange curves) the total spin signal and the spin polarizations along *x*, *y* and *z*. **e**, Projection on the *xy*-plane of the resulting 3D spin vectors around E_F. The circles represent the two Fermi surfaces of the light subbands. Arrows represent the measured polarization amplitude of pairs of opposite spin vectors around E_F, obtained from the fits to the spin signal with $|P_{fit}| = 1$. **f–j** same as **a–e** at an energy $E_F - 130$ meV, green dashed line in **f**. Note the decrease of measured polarization amplitude for the spins winding around the inner subband. **k–o** same as **a–e** at $E_F - 190$ meV purple dashed line in **k**. The measured polarization amplitude of the spins in the outer subband drops to 80% of its value around E_F. All data in this figure were measured at $h\nu = 47$ eV on the Γ_{102} Brillouin zone using linear-vertical photon polarization, at a temperature of 20 K.

antiparallel (down) to the local (that is, momentum-dependent) spin quantization axis **Q** (determined below and further discussed in Supplementary Note 2). Figure 1d shows the resulting spin polarization along **Q** as a function of electron momentum along (010). Figure 1f,g shows the corresponding spin-resolved data for electron momentum along the (100) direction.

The data in Fig. 1 demonstrate that the two light subbands are spin-polarized, with each band showing opposite spin orientations at opposite Fermi momenta—in other words, there is a spin-momentum locking causing a non-trivial spin texture. Indeed, the momentum separation at E_F between opposite spin states, given directly by the data in Fig. 1c,f, is equal to the difference in Fermi momenta between the two subbands—namely, about 0.1 Å^{-1}.

To further understand the spin-resolved data and determine **Q**, we analysed the momentum distribution curves (MDCs) at different binding energies. Thus, we fitted simultaneously the total spin-integrated MDC and the spin polarizations along the local *x* (tangential to the Fermi surface), *y* (radial) and *z* (out-of-plane) axes using a well-established quantitative vectorial analysis routine[19]. For definiteness, we concentrate on the subband dispersions along the (010) direction. These are shown again, for clarity in the discussion, in the colour plots of Fig. 2a,f,k. For measurements at the Fermi level, presented in Fig. 2a–d, the results of such fits are plotted as orange lines on top of the symbols showing the spin-integrated (Fig. 2a) and spin-resolved (Fig. 2b–d) data. From these measurements and fits, it can be concluded that each light subband is spin-polarized at the Fermi level, and that the spin vectors wind tangentially to the Fermi contours, with only a small out-of-plane component. Figure 2e shows the projection along *x* of the 3D spin-polarization vectors around E_F, obtained from the above data analysis. The amplitude of each spin-polarization vector, given by the fits, is $|P_{fit}| = 1$. This means that the detected free electrons photoemitted from the surface, whose spin polarization is well defined, have all spins essentially oriented along the same direction, tangential to the Fermi surface. These measured spin splittings and polarizations are robust with respect to changes in photon energy and polarization (see below and Supplementary Note 3), supporting the interpretation as an intrinsic spin structure of the light subbands[20].

Figure 2f–i shows the analysis of the spin-integrated and spin-resolved data taken around $E = -130$ meV. In this case, we find a reduced measured polarization vector length (40%) for the inner band, and a fully polarized (100%) outer band, as summarized in Fig. 2j. Likewise, the fits to data taken at $E = -190$ meV, presented in Fig. 2k–n, demonstrate that the degree of measured polarization of the outer subband decreases to 80% when approaching the band minimum, as seen from the corresponding spin vectors plotted in Fig. 2o. Thus, at this latter energy, a cut through the entire surface Brillouin zone consists of only a single spin-polarized contour.

Now, a crucial difference between the spin-split electronic structure measured here for the $SrTiO_3$ surface and a typical Rashba system is the absence, in our case, of a band crossing at $\mathbf{k}=0$ (refs 12,13,15)—see, for instance, the experimental band dispersions in Figs 1e and 2a. Note that, under time-reversal symmetry, electron eigenstates $E(\mathbf{k},\uparrow)$ of energy E, momentum $\mathbf{k}$ and spin $\uparrow$, transform into $E(-\mathbf{k},\downarrow)$, meaning that for $\mathbf{k}=0$ the bands should be degenerate. The absence of this Dirac point in our data points to a further unique property of the $SrTiO_3$ surface, namely the coexistence of a spin splitting of helical texture and some form of magnetism. Indeed, an out-of-plane component of an intrinsic magnetic moment can lift the above degeneracy and open up an additional gap for all momenta, including around $\mathbf{k}=0$ (ref. 21). Note also that our experiments were done in zero external magnetic field, to conserve the electron wavevector, essential for momentum-resolved measurements.

Thus, the combination of helical spin texture and magnetism with a sizeable component along the z-direction should lead to the occurrence of an out-of-plane spin polarization P_z of increasing amplitude close to the bottom of the band, as observed for topological insulators[22]. However, in the absence of an external magnetic field, both magnetic orientations along the z-axis are equally probable, and P_z will average to zero in macroscopic measurements such as SARPES. The total spin, however, is conserved and any canting of the spin along $\pm z$, implying the occurrence of domains with spin polarizations $\pm P_z$ in that direction, will result in a reduced component of the measured in-plane spin polarization. This is indeed compatible with the binding-energy-dependent SARPES measurements discussed in Fig. 2.

Therefore, all the data of Fig. 2 show that the spin polarization and winding on each subband are maintained down to the lowest binding energies. Note, in particular, that the spin texture of the outer subband retains a large in-plane polarization amplitude even in the gap between the two subbands, from about $E=-130$ meV to $E=-190$ meV. This suggests that the mechanism responsible for the helical in-plane spin texture is the main energy scale at large momenta. This energy scale is then one order of magnitude larger than both the one so far reported in $LaAlO_3/SrTiO_3$ interfaces[10,11], and the one expected from a naive Rashba model that takes solely into account the confining electric field. Such a strong deviation from the original Rashba scenario has been demonstrated for model metallic systems by numerous previous works[23,24], and is attributed as a general property of the surface corrugation and the associated wavefunction asymmetry[23–26], which results in a greatly enhanced Rashba parameter that increases the spin splitting. Thus, the large spin splitting of helical spin texture observed in our data may signal the relevance of surface corrugations for understanding the electronic and spin structure of the 2DEG at the surface of $SrTiO_3$.

Figure 3 is a schematic summary of our findings for the electronic structure of the light subbands at the surface of $SrTiO_3$. As shown by the illustration in Fig. 3a, these light subbands can be depicted in terms of coexisting Rashba and Zeeman splittings, with the first dominating at large momenta, and the second dominating around $\mathbf{k}=0$. In Fig. 3a, the sombrero-like form of the bottom of the lower band has been largely exaggerated: even for Rashba splittings comparable to the magnetic splitting at $\mathbf{k}=0$, one would obtain two almost parabolic bands (Supplementary Note 4). We thus stress that Fig. 3a is an oversimplified image, whereas our results and conclusions are dictated solely by the data, and are independent of any theoretical model or analysis.

To facilitate the remaining discussion, we label from 1 to 4 each of the subband branches, as shown in Fig. 3a. We also introduce, in Fig. 3b, the local $\{xyz\}$ axes and a schematic polar representation of the 3D spin vectors. Thus, we show in Fig. 3c–f the 3D spin vectors at E_F for the light subbands of the 2DEG at the surface of $SrTiO_3$, obtained from four different sets of measurements at various photon energies and polarizations. Data and fits corresponding to these measurements are presented in Supplementary Note 3.

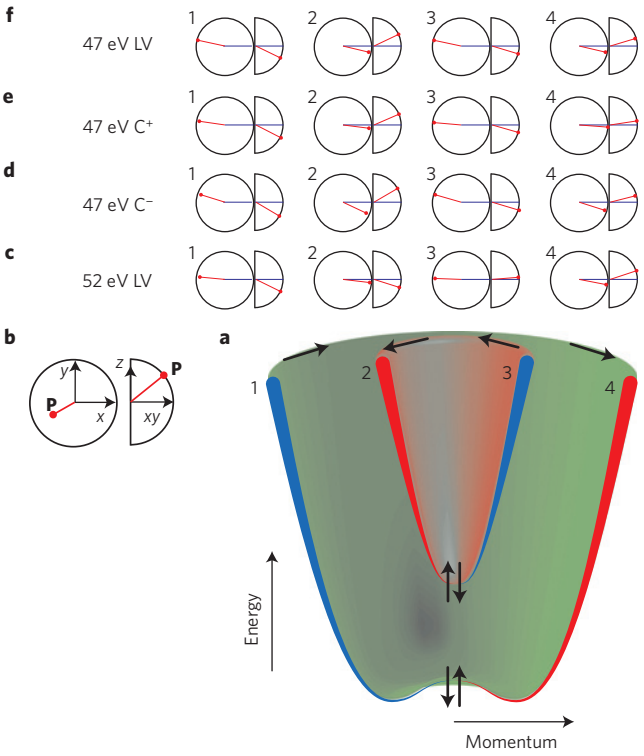

Figure 3 | Summary of spin splittings and spin vectors of the light subbands at the surface of $SrTiO_3$. a, Schematic representation of the spin-split light subbands at the surface of $SrTiO_3$. A number is assigned to each of the subband branches. The two subbands are separated by an energy gap of about 100 meV for all momenta from $\mathbf{k}=0$ to k_F. Each subband is spin-polarized, with spins winding in opposite directions for opposite momenta at a given binding energy. This is depicted by the arrows and the red and blue hues in different subband branches. For each band, the measured in-plane spin polarization decreases as one approaches the bottom of the band, and is schematically represented by the width of the parabolae. **b**, Definition of the local $\{xyz\}$ axes and polar representation of the 3D spin vectors (red ball-pointed arrows) used in the remaining plots of this figure. **c–f**, 3D spin vectors at E_F for each of the subband branches (1–4), obtained from four different sets of measurements at respectively $h\nu=52$ eV using linear-vertical (LV) photons, and at $h\nu=47$ eV using circular left-handed (C^-), circular right-handed (C^+), and LV photons. All data presented in this figure were measured on the Γ_{102} Brillouin zone at 20 K.

As seen from Fig. 3c–f, all the different measurements give consistent polarization vectors, although all sets were fitted independently. Note, in particular, that, for each of the subband branches, P_x is compatible between all the data sets, which furthermore show systematically the opposite non-trivial spin-winding textures for the inner and outer light bands. These results prove that the helical spin structure, the giant spin splitting, and the subband spin polarization reported in this work, are all independent of the photon energy and polarization and, hence, inherent to the electronic structure of the 2DEG at the surface of $SrTiO_3$(ref. 20). On the other hand, contrary to P_x, which does not change with photon energy or polarization, the out-of-plane component (P_z) of the spin polarization for the inner subband presents an anomaly (it gets inverted) at $h\nu=52$ eV. This suggests that P_z originates from extrinsic matrix elements of the SARPES process (Supplementary Note 3).

The possibility that the two light subbands of the 2DEG in $SrTiO_3$ are oppositely spin-polarized had been overlooked in previous

works[12,13,15], mainly for two reasons mentioned earlier. First, the splitting of the spin-polarized state, namely ~0.1 Å^{-1}, or about 100 meV at E_F, is unexpectedly large. Second, and perhaps even more surprisingly, the non-degenerate state of these two subbands at the Brillouin zone centre is not expected in a pure Rashba scenario, and implies the existence of a heretofore unobserved magnetic order associated with the metallic surface. In fact, although these two light subbands show very different photoemission selection rules on illumination with orthogonal photon polarizations, suggesting that they originate from orthogonal 3*d* orbitals[12], the Fermi surfaces they generate are both perfectly circular, indicating that they have the same d_{xy} orbital character[13,15]. These apparently contradictory observations of previous works can be reconciled by considering one crucial element—spin—that had been overlooked up to now: note that the total symmetry of each confined state is given by both the orbital and spinor parts of its wavefunction. Thus, our data demonstrate that the two light subbands at the surface of $SrTiO_3$ correspond to two d_{xy}-like bands, but with the spins of the electrons in each band locked to their momenta in opposite winding patterns. In other words, these subbands differ fundamentally in the symmetry of their total spin–orbital wavefunctions.

Our data are the first, direct demonstration of a non-trivial spin texture showing both a giant spin splitting and magnetism in the 2DEG at the bare surface of $SrTiO_3$ or any other oxide. In the case of $SrTiO_3$-based heterostructures, where ferromagnetism has been previously reported[7–9], recent X-ray magnetic circular dichroism experiments found it to arise from d_{xy} orbitals of Ti^{3+} character[27], and to be quenched by annealing in oxygen, suggesting a decisive role of oxygen vacancies in this phenomenon[28]. Interestingly, theoretical calculations have found that clusters of oxygen vacancies could induce an orbital reconstruction, generating an interfacial magnetic state with a dominant contribution from the d_{xy} states to the magnetic moment and an exchange energy splitting as large as a fraction of an eV (refs 29,30). Alternative models, based the interfacial splitting of t_{2g} orbital degeneracy in combination with electron correlations, have also been proposed[2,31–34].

It is interesting to contrast our findings with the case of spin-polarized quantum well states in ultrathin films of non-magnetic materials grown on ferromagnetic surfaces, such as, for example, Cu/Co(001) (refs 35,36). In the latter case, the spin polarization of the bands in the non-magnetic overlayer is induced by their interaction with the magnetic states in the substrate[35,36], and is of trivial ferromagnetic type—that is, the spin vectors are parallel for opposite momenta. In the case of $SrTiO_3$, on the other hand, the bulk material is merely a transparent paramagnetic band insulator at all temperatures, whereas the 2DEG at its surface shows both a non-trivial helical spin texture and magnetism. These original spin-polarized states must then clearly arise from intrinsic properties of the 2DEG and the spatial region where it is confined.

Thus, in analogy with the case of magnetism in $SrTiO_3$-based heterostructures, we speculate that for the 2DEG at the bare $SrTiO_3$ surface not only the surface-induced translational-symmetry breaking and subband orbital ordering[12], but also oxygen vacancies[12,13], and possibly lattice distortions[37] and/or electron exchange correlations, may play a fundamental role in establishing the observed non-trivial magnetic ground state. The exploration of all these possibilities, and the microscopic explanation of our observations, are at this point open issues beyond the scope of this work, and should be the subject of future theoretical and experimental research.

In a broader perspective, the spin structure unveiled by our data has far reaching consequences both for applications and for fundamental physics. $SrTiO_3$ represents the first example of a system with a large spin splitting at the Fermi level, four times larger than room temperature, located on a truly insulating substrate. This opens promising avenues for the realization of oxide-based spintronic devices. In addition, an exciting possibility would be tuning the Fermi level, for instance by chemical doping of the surface or by field effect, to lie exactly within the gap between the two spin-polarized subbands, yielding a single Fermi contour where the spin orientations are locked to the momenta. Such a spin structure, in conjunction with superconductivity, which occurs below 250 mK in $SrTiO_3$ (ref. 38) and $LaAlO_3/SrTiO_3$ heterostructures[5] for certain doping regimes, are the key ingredients for achieving the hotly pursued Majorana fermion. Such a scenario would be the 2D analogue of 1D InSb nanowires, where Majorana-like point modes were observed in proximity to a superconductor[39]. Given the rich phase diagrams of complex metallic oxides, and the spin structure observed here on $SrTiO_3$, oxide surface states now emerge as promising systems leading towards new physics and functionalities.

Methods

To realize TiO_2-terminated surfaces, the (001)-oriented $SrTiO_3$ crystals (SurfaceNet GmbH) were etched in a HF solution, and then annealed *ex situ* for 1 h at 1,000 °C in flowing oxygen. The samples were then transferred to an ultrahigh vacuum chamber, and reannealed in an oxygen atmosphere of 100 mbar at 500 °C for one hour. The surface quality was simultaneously monitored by reflection high-energy electron diffraction (RHEED), clearly showing the 1×1 diffraction pattern of the $SrTiO_3$-(001) surface. This treatment was followed by a second ultrahigh vacuum annealing (10^{-10} mbar) at 250–300 °C. The whole procedure yields transparent samples with conducting surfaces, as confirmed by the absence of charging effects in low-energy electron diffraction (LEED), STM and ARPES measurements (15). The samples were finally transferred to the SARPES station without breaking the ultra-high vacuum.

The SARPES experiments were done at the COPHEE end-station of the SIS beamline[40], Swiss Light Source (SLS), using linearly and circularly polarized photons in the energy range 30–80 eV, and an Omicron EA 125 hemispherical energy analyser equipped with two orthogonally mounted classic Mott detectors. These detectors, based on the spin–orbit scattering of the incident electron beam off a gold target, allow measurement of the electron spin without using an applied magnetic field, which would otherwise affect the momentum vector of the outgoing photoelectrons. The whole set-up allows the simultaneous measurements of all three spatial components of the spin-polarization vector for each point of the band structure. In this work, we concentrated on measuring spin-resolved MDCs, as they allow a direct, immediate visualization of both the spin splitting at different momenta and the spin texture around different Fermi surfaces. The angular and energy resolutions in spin-resolved mode were 1.5° and 60 meV, respectively. In spin-integrated mode the resolutions were set to 0.5° and 20 meV. The incident photon beam was smaller than $200 \times 200\,\mu m$ and $200 \times 800\,\mu m$ for the spin-integrated and spin-resolved measurements, respectively. All data were taken at $T = 20$ K. The results were reproduced on four samples over three different experimental runs.

Received 29 January 2014; accepted 5 September 2014; published online 12 October 2014

References

1. Ohtomo, A. & Hwang, H. Y. A high-mobility electron gas at the $LaAlO_3/SrTiO_3$ heterointerface. *Nature* **427,** 423–426 (2004).
2. Okamoto, S. & Millis, A. J. Electronic reconstruction at an interface between a Mott insulator and a band insulator. *Nature* **428,** 630–633 (2004).
3. Hwang, H. Y. *et al.* Emergent phenomena at oxide interfaces. *Nature Mater.* **11,** 103–113 (2012).
4. Thiel, S., Hammerl, G., Schmehl, A., Schneider, C. W. & Mannhart, J. Tunable quasi-two-dimensional electron gases in oxide heterostructures. *Science* **313,** 1942–1945 (2006).
5. Reyren, N. *et al.* Superconducting interfaces between insulating oxides. *Science* **317,** 1196–1199 (2007).
6. Ueno, K. *et al.* Electric-field-induced superconductivity in an insulator. *Nature Mater.* **7,** 855–858 (2008).
7. Brinkman, A. *et al.* Magnetic effects at the interface between non-magnetic oxides. *Nature Mater.* **6,** 493–496 (2007).
8. Li, L., Richter, C., Mannhart, J. & Ashoori, R. C. Coexistence of magnetic order and two-dimensional superconductivity at $LaAlO_3/SrTiO_3$ interfaces. *Nature Phys.* **7,** 762–766 (2011).
9. Bert, J. A. *et al.* Direct imaging of the coexistence of ferromagnetism and superconductivity at the $LaAlO_3/SrTiO_3$ interface. *Nature Phys.* **7,** 767–771 (2011).
10. Caviglia, A. D. *et al.* Tunable Rashba spin–orbit interaction at oxide interfaces. *Phys. Rev. Lett.* **104,** 126803 (2010).

11. Ben Shalom, M., Ron, A., Palevski, A. & Dagan, Y. Shubnikov-De Haas oscillations in $SrTiO_3/LaAlO_3$ interfaces. *Phys. Rev. Lett.* **105,** 206401 (2010).
12. Santander-Syro, A. F. *et al.* Two-dimensional electron gas with universal subbands at the surface of $SrTiO_3$. *Nature* **469,** 189–193 (2011).
13. Meevasana, W. *et al.* Creation and control of a two-dimensional electron liquid at the bare $SrTiO_3$ surface. *Nature Mater.* **10,** 114–118 (2011).
14. Santander-Syro, A. F. *et al.* Orbital symmetry reconstruction and strong mass renormalization in the two-dimensional electron gas at the surface of $KTaO_3$. *Phys. Rev. B* **86,** 121107 (2012).
15. Plumb, N. C. *et al.* Mixed dimensionality of confined conducting electrons in the surface region of $SrTiO_3$. *Phys. Rev. Lett.* **113,** 086801 (2014).
16. Khalsa, G., Lee, B. & MacDonald, A. H. Theory of t_{2g} electron-gas Rashba interactions. *Phys. Rev. B* **88,** 041302(R) (2013).
17. Zhong, Z., Zhang, Q. & Held, K. Quantum confinement in perovskite oxide heterostructures: Tight binding instead of a nearly free electron picture. *Phys. Rev. B* **88,** 125401 (2013).
18. Winkler, R. *Spin–Orbit Coupling Effects in Two-Dimensional Electron and Hole Systems* (Springer, 2003).
19. Meier, F., Dil, J. H. & Osterwalder, J. Measuring spin polarization vectors in angle-resolved photoemission spectroscopy. *New J. Phys.* **11,** 125008 (2009).
20. Heinzmann, U. & Dil, J. H. Spin–orbit-induced photoelectron spin polarization in angle-resolved photoemission from both atomic and condensed matter targets. *J. Phys. Condens. Matter* **24,** 173001 (2012).
21. Potter, A. C. & Lee, P. A. Multichannel generalization of Kitaev's Majorana end states and a practical route to realize them in thin-films. *Phys. Rev. Lett.* **105,** 227003 (2010).
22. Xu, S-Y. *et al.* Hedgehog spin texture and Berry's phase tuning in a magnetic topological insulator. *Nature Phys.* **8,** 616–622 (2012).
23. Dil, J. H. Spin and angle resolved photoemission on non-magnetic low-dimensional systems. *J. Phys. Condens. Matter* **21,** 403001 (2009).
24. Gierz, I. *et al.* Structural influence on the Rashba-type spin splitting in surface alloys. *Phys. Rev. B* **81,** 245430 (2010).
25. Bihlmayer, G., Koroteev, Y. M., Echenique, P. M., Chulkov, E. V. & Blügel, S. The Rashba effect at metallic surfaces. *Surf. Sci.* **600,** 3888–3891 (2006).
26. Nagano, M., Kodama, A., Shishidou, T. & Oguchi, T. A first-principles study on the Rashba effect in surface systems. *J. Phys. Condens. Matter* **21,** 064239 (2009).
27. Lee, J-S. *et al.* Titanium d_{xy} ferromagnetism at the $LaAlO_3/SrTiO_3$ interface. *Nature Mater.* **12,** 703–706 (2013).
28. Salluzzo, M. *et al.* Origin of interface magnetism in $BiMnO_3/SrTiO_3$ and $LaAlO_3/SrTiO_3$ heterostructures. *Phys. Rev. Lett.* **111,** 087204 (2013).
29. Pavlenko, N., Kopp, T., Tsymbal, E. Y., Mannhart, J. & Sawatzky, G. A. Oxygen vacancies at titanate interfaces: Two-dimensional magnetism and orbital reconstruction. *Phys. Rev. B* **86,** 064431 (2012).
30. Pavlenko, N., Kopp, T., Tsymbal, E. Y., Sawatzky, G. A. & Mannhart, J. Magnetic and superconducting phases at the $LaAlO_3/SrTiO_3$ interface: The role of interfacial Ti 3*d* electrons. *Phys. Rev. B* **85,** 020407(R) (2012).
31. Michaeli, K., Potter, A. C. & Lee, P. A. Superconducting and ferromagnetic phases in $SrTiO_3/LaAlO_3$ oxide interface structures: Possibility of finite momentum pairing. *Phys. Rev. Lett.* **108,** 117003 (2012).
32. Banerjee, S., Erten, O. & Randeria, M. Ferromagnetic exchange, spin–orbit coupling and spiral magnetism at the $LaAlO_3/SrTiO_3$ interface. *Nature Phys.* **9,** 626–630 (2013).
33. Okamoto, S., Millis, A. J. & Spaldin, N. A. Lattice relaxation in oxide heterostructures: $LaTiO_3/SrTiO_3$ superlattices. *Phys. Rev. Lett.* **97,** 056802 (2006).
34. Pentcheva, R. & Pickett, W. E. Ionic relaxation contribution to the electronic reconstruction at the *n*-type $LaAlO_3/SrTiO_3$ interface. *Phys. Rev. B* **78,** 205106 (2008).
35. Garrison, K., Chang, Y. & Johnson, P. D. Spin polarization of quantum well states in copper thin films deposited on a Co(001) substrate. *Phys. Rev. Lett.* **71,** 2801–2804 (1993).
36. Carbone, C., Vescovo, E., Rader, O., Gudat, W. & Eberhardt, W. Exchange split quantum well states of a noble metal film on a magnetic substrate. *Phys. Rev. Lett.* **71,** 2805–2808 (1993).
37. Bickel, N., Schmidt, G., Heinz, K. & Müller, K. Ferroelectric relaxation of the $SrTiO_3$(100) surface. *Phys. Rev. Lett.* **62,** 2009–2011 (1989).
38. Schooley, J. F., Hosler, W. R. & Cohen, M. L. Superconductivity in semiconducting $SrTiO_3$. *Phys. Rev. Lett.* **12,** 474–475 (1964).
39. Mourik, V. *et al.* Signatures of Majorana fermions in hybrid superconductor–semiconductor nanowire devices. *Science* **336,** 1003–1007 (2012).
40. Hoesch, M. *et al.* Spin-polarized Fermi surface mapping. *J. Electron Spectrosc. Relat. Phenom.* **124,** 263–279 (2002).

Acknowledgements

We thank M. Gabay, M. Rozenberg, N. Reyren, R. Claessen, S. Ming, L. Patthey and J. Mesot for discussions. Experiments were conducted at the Surface/Interface Spectroscopy (SIS) beamline of the Swiss Light Source within the Paul Scherrer Institut in Villigen, Switzerland. The COPHEE end-station is supported by the Swiss National Science Foundation. Work at the CSNSM is supported by public grants from the French National Research Agency (ANR) (project LACUNES No ANR-13-BS04-0006-01) and the 'Laboratoire d'Excellence Physique Atomes Lumière Matière' (LabEx PALM project ELECTROX) overseen by the ANR as part of the 'Investissements d'Avenir' program (reference: ANR-10-LABX-0039). T.C.R. is supported by the RTRA–Triangle de la Physique (project PEGASOS). J.H.D. acknowledges support from the Swiss National Science Foundation. A.F.S-S. acknowledges support from the Institut Universitaire de France.

Author contributions

Project conception: A.F.S-S., F.F., J.H.D. and M.R.; measurements: A.F.S-S., F.F., C.B., T.C.R., G.L., N.C.P., J.H.D. and M.R.; infrastructure for SARPES experiments at SLS: G.L. and J.H.D.; sample characterizations: N.C.P. and M.R.; data analysis: A.F.S-S., F.F. and J.H.D.; writing of the manuscript: A.F.S-S., F.F. and J.H.D. All authors extensively discussed the results and the manuscript.

Additional information

Supplementary information is available in the online version of the paper. Reprints and permissions information is available online at www.nature.com/reprints. Correspondence and requests for materials should be addressed to A.F.S-S., J.H.D. or M.R.

Competing financial interests

The authors declare no competing financial interests.